

OPEN ACCESS

Study of the Failure Mechanisms of $\text{LiNi}_{0.8}\text{Mn}_{0.1}\text{Co}_{0.1}\text{O}_2$ Cathode Material for Lithium Ion Batteries

To cite this article: Jing Li *et al* 2015 *J. Electrochem. Soc.* **162** A1401

View the [article online](#) for updates and enhancements.

You may also like

- [A Comparison of the Performance of Different Morphologies of \$\text{LiNi}_{0.8}\text{Mn}_{0.1}\text{Co}_{0.1}\text{O}_2\$ Using Isothermal Microcalorimetry, Ultra-High Precision Coulometry, and Long-Term Cycling](#)
E. R. Logan, Helena Hebecker, Xiaowei Ma *et al.*
- [The Impact of Electrolyte Additives and Upper Cut-off Voltage on the Formation of a Rocksalt Surface Layer in \$\text{LiNi}_{0.8}\text{Mn}_{0.1}\text{Co}_{0.1}\text{O}_2\$ Electrodes](#)
Jing Li, Hanshuo Liu, Jian Xia *et al.*
- [Exploring Interactions between Electrodes in \$\text{Li}|\text{Ni}_x\text{Mn}_y\text{Co}_z|\text{IO}_2/\text{Graphite}\$ Cells through Electrode/Electrolyte Interfaces Analysis](#)
Lénaïc Madec and Leah D. Ellis



Your Lab in a Box!

The PAT-Tester-i-16: All you need for Battery Material Testing.

- ✓ All-in-One Solution with integrated Temperature Chamber!
- ✓ Cableless Connection for Battery Test Cells!
- ✓ Fully featured Multichannel Potentiostat / Galvanostat / EIS!

www.el-cell.com +49 40 79012-734 sales@el-cell.com

EL-CELL[®]
electrochemical test equipment





Study of the Failure Mechanisms of $\text{LiNi}_{0.8}\text{Mn}_{0.1}\text{Co}_{0.1}\text{O}_2$ Cathode Material for Lithium Ion Batteries

Jing Li,^a Laura E. Downie,^{b,*} Lin Ma,^{c,*} Wenda Qiu,^d and J. R. Dahn^{a,b,c,**,z}

^aDepartment of Process Engineering and Applied Science, Dalhousie University, Halifax, NS B3H 3J5, Canada

^bDepartment of Physics and Atmosphere Science, Dalhousie University, Halifax, NS B3H 3J5, Canada

^cDepartment of Chemistry, Dalhousie University, Halifax, NS B3H 3J5, Canada

^dSchool of Chemistry and Chemical Engineering, Sun Yat-Sen University, Guangzhou 510275, People's Republic of China

$\text{LiNi}_{0.8}\text{Mn}_{0.1}\text{Co}_{0.1}\text{O}_2$ (NMC811) can deliver a high capacity of ~ 200 mAh/g with an average discharge potential of ~ 3.8 V (vs. Li^+/Li), making it a promising positive electrode material for high energy density lithium ion batteries. However, electrochemical tests from half cells and full cells show poor cycling performance when charged to potentials above 4.2 V. The calendar and cycle lifetimes of cells are affected by the structural stability of the active electrode materials as well as the parasitic reactions that occur in lithium ion batteries. In order to explore the major failure mechanisms of the material, half cells (coin cells) with control electrolyte and full cells (pouch cells) with control electrolyte and with selected electrolyte additives were tested over four different potential ranges. Isothermal microcalorimetry was used to explore the parasitic reactions and their potential dependence. In-situ and ex-situ X-ray diffraction and scanning electron microscopy were used to investigate the structural and morphological degradation of the materials over cycling. It was found that the dramatic c-axis change of the active material during charge and discharge may not be the major problem for cells that are cycled to higher potentials. The parasitic reactions that arise from the interactions between the electrolyte and the highly reactive delithiated cathode surface at high potentials are suggested as the main reason for the failure of cells cycled above 4.2 V. It should be possible to further improve the performance of NMC811 at high potentials by modifying the cathode surface and/or identifying and using electrolyte blends which reduce parasitic reactions.

© The Author(s) 2015. Published by ECS. This is an open access article distributed under the terms of the Creative Commons Attribution 4.0 License (CC BY, <http://creativecommons.org/licenses/by/4.0/>), which permits unrestricted reuse of the work in any medium, provided the original work is properly cited. [DOI: 10.1149/2.1011507jes] All rights reserved.

Manuscript submitted March 25, 2015; revised manuscript received April 16, 2015. Published April 30, 2015.

High energy density lithium ion batteries (LIBs) that are cheaper, safer, and with longer lifetimes need to be developed in order to meet the increasing demand for applications such as electric vehicles and large scale stationary energy storage. The energy density of LIBs can be increased by increasing the specific capacity and average potential of the cells. The calendar and cycle lifetimes of cells are affected by the structural stability of the active electrode materials as well as the parasitic reactions that occur in lithium ion batteries. The degree of lithium utilization of LiCoO_2 is limited to $\sim 70\%$ in order to avoid the O3 – H1-3 – O1 phase transformation when charged above 4.45 V.¹ Parasitic reactions such as electrolyte oxidation at the cathode-electrolyte interface can ultimately cause cell failure.^{2–5} The rate of the parasitic reactions is related to both the catalytic role of the cathode surface which depends on its composition and surface area,^{3,6} as well as on the stability of the electrolyte.^{2–5} Methods such as the use of electrolyte additives^{7–11} and core-shell positive electrode materials^{12–14} have been developed and studied to reduce the rate and extent of parasitic reactions, and hence increase capacity retention and lifetime of high-voltage Li-ion cells.

The layered lithium Ni-Mn-Co oxides $\text{Li}_{1-x}(\text{Ni}_y\text{Mn}_z\text{Co}_{(1-y-z)})_{1-x}\text{O}_2$ (NMC) are considered to be promising positive electrode materials.^{15–23} In our previous report²⁴ and in numerous literature reports,^{6,14,16,17,19,25–32} it has been shown that the electrochemical performance of these lithium-rich layered materials is dependent on their structure and composition. The lithium-rich manganese-rich NMC materials with excess lithium in the transition metal layer can have extraordinary high specific capacity of more than 250 mAh/g with an average potential of ~ 3.6 V (vs. Li^+/Li) after an irreversible oxygen release activation process at ~ 4.5 V (vs. Li^+/Li).^{19,22,23} However, to obtain such a capacity, these materials must be cycled over a wide potential range of 2.5–4.6 V (vs. Li^+/Li), which may be challenging for the current carbonate-based electrolytes. Major issues such as large irreversible capacity (IRC),^{19,33,34} voltage fade upon cycling^{22,35–40} and poor rate capability^{22,41,42} have hindered the application of these materials.

Conversely, Ni-rich oxides such as $\text{LiNi}_{0.8}\text{Mn}_{0.1}\text{Co}_{0.1}\text{O}_2$ (NMC811) can also deliver a high capacity of ~ 200 mAh/g with an average discharge potential of ~ 3.8 V (vs. Li^+/Li), but over a much narrower potential range of ~ 3 –4.4 V (vs. Li^+/Li), and have therefore drawn much attention.^{41,43–46} The main difficulty of synthesizing Ni-rich materials is the minimization of the degree of cation mixing which requires an excess of lithium source prior to sintering.²⁴ However, lithium compounds remaining after synthesis, like Li_2CO_3 , have a negative impact on the cell.^{43,47} It was shown that Ni-rich materials have poor charge-discharge capacity retention, which could be related to the electrolyte oxidation at the positive electrode surface^{7–9,48,49} and/or structural changes of the material, such as large c-axis shrinkage, at high potentials.^{43,46,50,51} This work is therefore aimed at determining the failure mechanism of NMC811 as a function of the potential range chosen for cycle testing, the results of which will aid in further developments.

In this work, half cells (coin cells) with control electrolyte and full cells (pouch cells) with control electrolyte plus additives such as vinylene carbonate (VC) and a prop-1-ene-1,3-sultone (PES) based blend were tested over four different upper cutoff potential ranges. Isothermal microcalorimetry was used to explore the parasitic reactions and their potential dependence while in-situ and ex-situ X-ray diffraction (XRD) and scanning electron microscopy (SEM) were used to investigate the structural degradation of the materials during cycling. Safety issues associated with the reactivity of the charged electrode material and electrolyte at elevated temperature were studied using accelerating rate calorimetry (ARC).

Experimental

Reagents used in this investigation included $\text{LiNi}_{0.8}\text{Mn}_{0.1}\text{Co}_{0.1}\text{O}_2$ (NMC811) (LiFun Technology, Hunan, China), N-methylpyrrolidone (NMP, 99.5%, Sigma-Aldrich), poly(vinylidene) fluoride (PVDF, Kynar 301F, Arkema), Super-S carbon black (Timcal), 1:2 v/v ethylene carbonate:diethyl carbonate (EC:DEC) (BASF), lithium hexafluorophosphate (LiPF_6) (BASF, 99.9%). Vinylene carbonate (VC) (BASF, 99.97%), prop-1-ene-1,3-sultone (PES) (Lianchuang Medicinal Chemistry Co., 98.20%), tris(trimethylsilyl)phosphite (TTSPI) (TCI America, > 95%), and methylene methanedisulfonate (MMDS)

*Electrochemical Society Student Member.

**Electrochemical Society Fellow.

^zE-mail: jeff.dahn@dal.ca

(Guangzhou Tinci Co. Ltd., 98.70%) were used as electrolyte additives.

Coin cells.— A slurry with a mixture of 92 wt% active material, 4 wt% Super-S carbon black and 4 wt% PVDF with NMP as the solvent were first prepared. Electrodes were made by coating the slurry on an Al foil with a 150 μm notch bar spreader, which were pressed with a pressure of 200 psi after dried in air. The electrodes were dried overnight at 120°C in a vacuum oven before use. The electrolyte used was 1.0 M LiPF₆ in 1:2 v/v ethylene carbonate:diethyl carbonate (EC:DEC). The separators used were one Celgard 2320 (Celgard) on the lithium electrode and one polypropylene blown-microfiber separator (3M) adjacent to the positive electrode. Galvanostatic charge/discharge cycling, using standard 2325 coin cells with lithium metal as the anode, was done using an E-One Moli Energy Canada battery testing system. All the cells were tested with a current density of 10 mA/g ($\sim C/20$) for one cycle and 40 mAh/g ($\sim C/5$) at the following cycles. Cells were tested between 3.0–4.1, 4.2, 4.3 or 4.4 V (vs. Li/Li⁺) at 30°C, respectively.

Pouch cells.— NMC811/graphite pouch cells (220 mAh) were obtained dry (no electrolyte) and sealed from LiFun Technology (Xinma Industry Zone, Golden Dragon Road, Tianyuan District, Zhuzhou City, Hunan Province, PRC, 412000). Details about the NMC811 can be found in Figure S1 and Table S1 in the supporting information. The cells were opened and placed in a heated vacuum oven at 80°C overnight (approximately 14 hours) to remove any residual water. After drying, the cells were directly transferred to an argon-filled glove box without exposure to ambient air, where they were filled with 0.90 g electrolyte.

The control electrolyte was 1M LiPF₆ in 3:7 v:v ethylene carbonate (EC):ethylmethyl carbonate (EMC) (BASF, max < 20 ppm water). Electrolyte additives used in this work were VC, PES, TTSPi and MMDS. The combinations of the above additives studied were 2 wt% VC and 2 wt% PES + 1 wt% MMDS + 1 wt% TTSPi (PES211). Once cells were filled with electrolyte, they were sealed with a compact vacuum sealer (MSK-115V, MTI Corp.) to 94% of full vacuum (−95.2 kPa gauge pressure or 6.1 kPa absolute pressure) with a 6 second sealing time at 165°C.

All cells were placed in a temperature-controlled box at 40. \pm 0.1°C and held at 1.5 V for 24 hours to ensure complete wetting. Then cells were charged at C/20 to 3.8 V using a Maccor series 4000 automated test system (Maccor Inc.), where C/20 is the current required to complete a full charge or discharge in 20 hours. The cells were transferred back to an argon-filled glove box and cut back open under the previous seal to release any gas that was produced. The cells were then vacuum sealed again as previously described. The cells were tested at C/20 for two cycles and followed by running at C/5 for 200 cycles at 30. \pm 0.1°C in temperature-controlled boxes.

Isothermal microcalorimetry.— Heat flow measurements were performed using a TAM III isothermal microcalorimeter (TA Instruments) as described in Ref. 48. All data were collected at 40.00°C with a heat flow measurement uncertainty of $< \pm 1.0 \mu\text{W}$, a noise level of about 100 nW, and a baseline drift from 0.00 μW to less than 500 nW over the experimental time frame. While inside the calorimeter, cells were charged and discharged using a Maccor series 4000 automated test system (Maccor Inc.). The NMC811/graphite cells were first left under open circuit conditions for 24 hours to allow for complete thermal equilibration. These cells were then charged and discharged between 2.8–4.1 V four times at 10 mA (C/20) to allow for partial stabilization of the SEI layers. The cells were then charged to 4.0 V at 10 mA, then proceeded through a charge-discharge segment between 4.0–4.1 V at 10 mA, then 5 mA, then 2 mA, then finally 1 mA. The cells were charged to 4.1 V at 10 mA, then proceeded through four charge-discharge segments between 4.1–4.2 V at 10 mA for partial SEI stabilization in that voltage range, then were cycled between the

same voltage limits for 10 mA, 5 mA, 2 mA, then finally 1 mA. This variable rate procedure was repeated for 4.2–4.3 V and 4.3–4.4 V.

In-situ X-ray diffraction.— In-situ X-ray diffraction was carried out using a Siemens D5000 diffractometer equipped with a Cu target X-ray tube and a diffracted beam monochromator. The aforementioned slurry, which was purposely made thicker with less NMP, was casted using a 660 μm notch bar directly onto a 2 cm diameter beryllium window. The electrodes were dried overnight at 120°C in a vacuum oven before use. The beryllium window was attached using Roscobond pressure sensitive adhesive to the positive electrode side of the cell case that had a pre-cut 1.5 cm diameter hole. The in-situ cell was then assembled in the same way as coin cells. The cell was cycled at a rate of C/100 between 3.0–4.4 V for two cycles using the E-one Moli charger system, while diffraction patterns were collected in the scattering angle (2θ) range of 17–20°, 35–50°, 57–60° and 62–70° at 0.05° intervals with a dwell time of 15 s. Each scan was approximately 2.5 h.

Ex-situ X-ray diffraction and scanning electron microscopy.— Pouch cells with electrolyte containing 2% VC were discharged to ~ 0 V after 200 cycles (between 3–4.1, 4.2, 4.3 or 4.4 V with a rate of C/5) and then disassembled. The electrodes were rinsed with dimethyl carbonate (DMC) (99%, Sigma) to remove any residual electrolyte. Ex-situ XRD was carried out using a zero-background silicon wafer sample holder. Diffraction patterns were collected using the same Siemens D5000 diffractometer discussed above, in the scattering angle (2θ) range of 15–70° at 0.05° intervals with a dwell time of 5 s.

Scanning Electron Microscopy (SEM) was carried out using a Hitachi S-4700 SEM equipped with a 80 mm² silicon drift detector at Dalhousie University.

Accelerating rate calorimetry (ARC).— The single-point BET surface areas of NMC811 and NMC111 (LiNi_{1/3}Mn_{1/3}Co_{1/3}O₂) powders were measured with a Micromeritics Flowsorb 2300 instrument and were found to be $0.38 \pm 0.01 \text{ m}^2/\text{g}$ and $0.48 \pm 0.01 \text{ m}^2/\text{g}$, respectively. Pellet-type electrodes were made with a weight ratio of active material: Super-S carbon black: PVDF binder of 92:4:4. Pellet-type electrode coin cells were made using control electrolyte and charged to 4.2 V using a “signature charge” protocol as described in Refs. 52 and 53. At 4.2 V the specific capacity of the NMC811 and NMC111 electrodes were $185 \pm 5 \text{ mAh/g}$ and $160 \pm 5 \text{ mAh/g}$, respectively. The coin cells were then opened in an argon-filled glove box. The electrode was ground lightly and rinsed four times using DMC to remove any residual electrolyte. The powder was then dried overnight in the vacuum antechamber of a glove box before being used for the ARC tests. 94 mg of delithiated NMC111 and 30 mg of electrolyte were used for the ARC tests. To keep the same capacity with NMC111 and the same ratio between electrode material and electrolyte, 81 mg delithiated NMC811 and 26 mg electrolyte were used during the ARC test. The ARC starting temperature was set at 70°C. ARC tests were tracked under adiabatic conditions when the sample self-heating rate (SHR) exceeded 0.03°C/min. Experiments were stopped at 350°C or when the SHR exceeded 20°C/min. To test the reproducibility of the ARC sample construction and measurements, two identical ARC samples were made and tested for every condition.

Results and Discussion

Figure 1a shows the voltage versus capacity curves of Li/NMC811 coin cells with an upper cutoff potential of 4.1 V in red, 4.2 V in blue, 4.3 V in yellow, and 4.4 V in black. For all cells, the electrolyte used was 1.0 M LiPF₆ in 1:2 v/v EC:DEC and the lower cutoff potential was 3.0 V. The cells were tested at C/20 for 2 cycles and then cycled at C/5 at a constant temperature of 30°C. The first charge curves in the range of 3.0–3.9 V show a different pathway than the second charge, whereas there is good overlap between the first and second charge pathways in the 3.9–4.4 V region. Irreversible capacities of

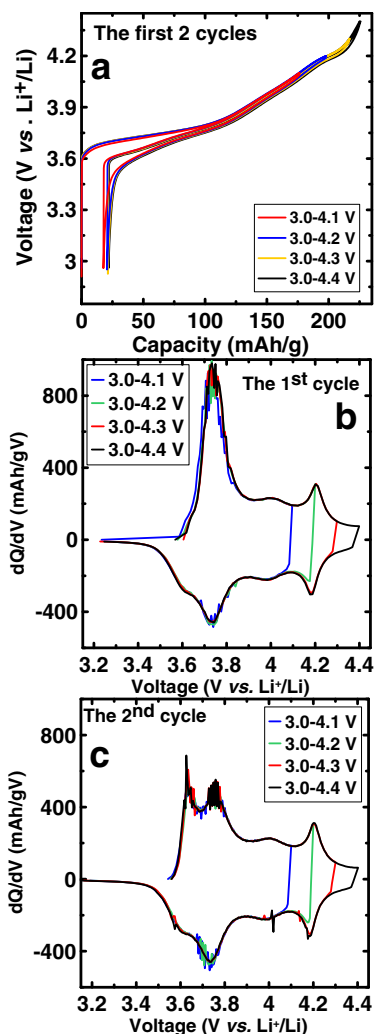


Figure 1. (a) The voltage versus capacity curves of NMC811/Li coin cells with an upper cutoff potential of 4.1 V, 4.2 V, 4.3 V and 4.4 V (vs. Li⁺/Li) respectively. (b) Differential capacity (dQ/dV) as a function of cell potential for the first cycle with the four upper cutoff potentials respectively. (c) Differential capacity (dQ/dV) as a function of cell potential for the second cycle with the four upper cutoff potentials respectively. The cells were tested at a rate of C/20 for 2 cycles and then cycled at a rate of C/5 under a constant temperature of 30°C.

about 20–25 mAh/g were observed and reversible capacities of 159, 178, 195, and 203 mAh/g from 3.0–4.1 V, 4.2 V, 4.3 V, and 4.4 V (vs. Li/Li⁺), respectively, were measured. The potential increased very rapidly between 4.3 V and 4.4 V such that the capacity in this range is only ~10 mAh/g.

Figure 1b shows the corresponding differential capacity (dQ/dV) as a function of cell potential for the first cycle for each of the four upper cutoff potentials. A weak charge peak at ~3.65 V and an intense charge peak at ~3.75 V, together with two charge peaks at ~3.95 V and ~4.2 V were observed. There were no obvious peaks between 4.3 and 4.4 V, which agrees well with the small capacity observed in this region.

Figure 1c shows the dQ/dV curves of the second cycle for each of the four upper cutoff potentials. A relatively more intense charge peak at ~3.65 V and a relatively weaker peak at ~3.75 V were measured when compared with the first charge. Conversely, there were no significant differences of the peaks at ~3.95 V and ~4.2 V between the first and second charge in the 3.9–4.4 V region. The corresponding discharge peaks at ~3.65 V, 3.75 V, 3.9 V, and 4.2 V match well with those observed for the first discharge.

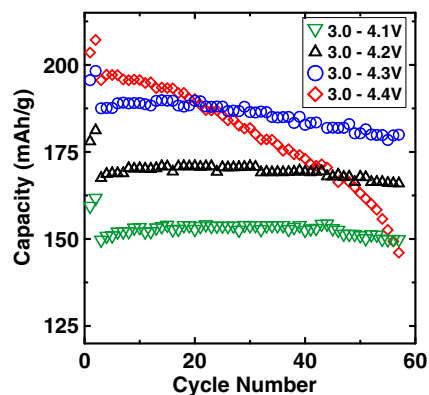


Figure 2. Discharge capacity of NMC811/Li coin cells with control electrolyte as a function of cycle number for four different potential ranges.

Figure 2 shows the measured discharge capacity of the Li/NMC811 coin cells as a function of cycle number. The cells tested with an upper cutoff potential of 4.1 V, 4.2 V, 4.3 V and 4.4 V (vs. Li/Li⁺) are shown in green inverted triangles, black triangles, blue circles and red diamonds, respectively. Second discharge capacities of ~161, 180, 198, and 207 mAh/g at C/20 were measured from 3.0–4.1 V, 4.2 V, 4.3 V and 4.4 V, respectively, whereas the second discharge capacities at C/5 within the same potential ranges were ~150, 169, 188 and 197 mAh/g respectively. After 57 cycles, measured capacities were 149, 166, 180, and 146 mAh/g with corresponding capacity retentions of 99%, 98%, 95% and 74% (comparing to the second discharge at C/5), respectively. Cells that cycled above 4.2 V showed poor capacity retention. Moreover, a very significant and discontinuous increase in capacity fade rate was observed between cells that were cycled between 3.0–4.3 V and 3.0–4.4 V, despite a small 0.1 V difference in upper cutoff potential.

Figure 3 shows the discharge capacity as a function of cycle number for NMC811 pouch cells (full cells) containing control electrolyte with 2% VC in red symbols and with PES211 in blue and black symbols. The cells were tested with a lower cutoff potential of 3.0 V for the 2% VC cells and 2.8 V for PES211 cells, while the upper cutoff potentials were 4.1 V, 4.2 V, 4.3 V and 4.4 V, respectively. The cells were cycled at C/20 for two cycles and then cycled at C/5 at 30°C for the duration of the experiment. Cells containing 2% VC had capacities of 167, 186, 177, and 161 mAh after 70 cycles, with corresponding capacity retentions of 98%, 98%, 91%, and 88% compared to the third cycle at 4.1 V, 4.2 V, 4.3 V and 4.4 V respectively. Cells containing PES211 had capacities of 154, 156, 163 and 148 mAh after only 40 cycles

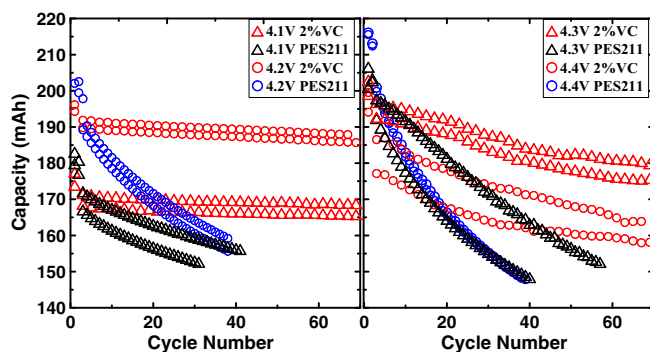


Figure 3. Discharge capacity of NMC811/graphite pouch cells with electrolyte additives in the control electrolyte as a function of cycle number. The cells were tested with a lower cutoff potential of 3.0 V for 2% VC cells and 2.8 V for PES211 cells, while the upper cutoff potentials were 4.1 V, 4.2 V, 4.3 V and 4.4 V for both electrolytes. The cells were cycled at a rate of C/20 for two cycles and then cycled at a rate of C/5 in a temperature box at 30°C.

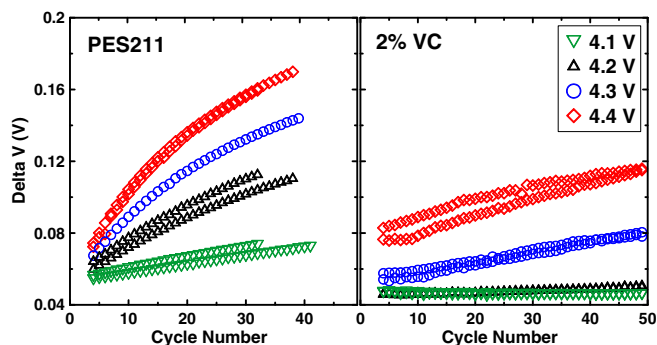


Figure 4. ΔV of the pouch cells as a function of cycle number. Cells with PES211 are shown in the left panel and cells with 2% VC are shown in the right panel.

with capacity retentions of 91%, 82%, 82% and 74% at 4.1 V, 4.2 V, 4.3 V and 4.4 V respectively. PES211 cells showed worse capacity retention compared with 2% VC cells cycled to the same potential. This surprised us because NMC442/graphite and NMC111/graphite cells with PES211 electrolyte show significantly **better** performance than cells with 2% VC,^{54,55} suggesting the Ni-rich surface of NMC811 behaves differently. Cells containing 2% VC cycled to and above 4.3 V showed much worse capacity retention performance compared to cells cycled to and below 4.2 V.

In order to explore what was happening inside the cells, the average polarization, ΔV , was calculated by subtracting the average charge potential and the average discharge potential. The average potential was determined by dividing the charge/discharge energy (Wh) by the charge/discharge capacity (Ah) respectively.

Figure 4 shows ΔV as a function of cycle number, which tracks the increase in the polarization of the cells. Cells cycled at lower potentials showed smaller initial ΔV , beginning at the fourth cycle. ΔV was found to be 0.046 V at 4.1 V, 0.046 V at 4.2 V, 0.056 V at 4.3 V and 0.079 V at 4.4 V for 2% VC cells, while it was 0.055 V at 4.1 V, 0.062 V at 4.2 V, 0.067 V at 4.3 V and 0.073 V for PES211 cells. Cells containing PES211 showed larger initial ΔV when cycled to a potential lower than 4.4 V comparing to 2% VC cells, indicating larger cell impedance. After 50 cycles, 2% VC cells at 4.1 V showed very stable ΔV of 0.045 V, while a small increase to ~ 0.051 V was observed for cells cycled to 4.2 V. Meanwhile, the ΔV increased rapidly to 0.086 V and 0.116 V for cells cycled at 4.3 V and 4.4 V respectively, suggesting significant impedance growth for cells cycled to higher potentials. Conversely, PES211 cells in general showed much larger increases in polarization with continued cycling. ΔV was 0.072 V, 0.114 V, 0.145 V, and 0.169 V after 40 cycles at 4.1 V, 4.2 V, 4.3 V, and 4.4 V respectively.

The observed impedance growth upon cycling could explain the poor cycling performance of 2% VC cells at higher potentials, as well as PES211 cells even at 4.1 V. The difference in the impedance growth rates shows that different electrolyte additives have different parasitic reaction rates and products which can significantly impact the cell performance.

In order to further examine the parasitic reaction rate of the cells with different electrolyte additives, cells with PES211 and 2% VC were tested with isothermal microcalorimetry and the data were analyzed. Figure 5 shows the extracted polarization, entropic, and parasitic heat flow components of the total heat flow as a function of the relative state of charge (rSOC) for 2% VC and PES211 pouch cells operating during charge at 5 mA. rSOC is defined as running from 0 to 1 over each potential range studied. For each of the four potential ranges explored, 4.0–4.1 V, 4.1–4.2 V, 4.2–4.3 V, and 4.3–4.4 V, the total measured heat flow was collected for four currents (charge and discharge), 10 mA, 5 mA, 2 mA, and 1 mA. The total measured heat flow for all currents was fit using a three-component model described by Downie et al.^{48,56} that included the irreversible heat flow due to

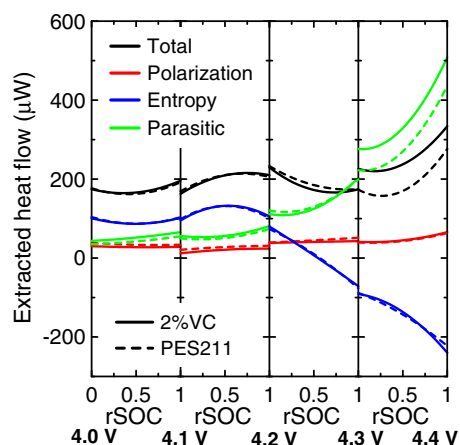


Figure 5. The extracted polarization (red), entropic (blue), and parasitic (green) heat flow components of the total heat flow (black) as a function of the relative state of charge (rSOC) for 2% VC (solid lines) and PES211 (dashed lines) cells for a 5 mA charge segment.

polarization, the reversible heat flow due to changes in entropy as a function of lithium content, and the time-dependent heat flow resulting from the sum of all parasitic reactions occurring in the cell. In this model, each contribution was described using a simple polynomial function of rSOC. The extracted fitting parameters then gave the relative contributions of each term as a function of rSOC. This method is described in detail in Refs. 48 and 56.

Figure 5 shows the extracted results for cells containing 2% VC in solid lines and PES211 in dashed lines for a 5 mA charge segment in each potential range. Both cells have similar heat flows due to polarization throughout the entire potential range examined during these early cycles. At 5 mA ($C/40$) the cell polarization is small, which is reflected in the magnitude of polarization heat flow. The heat flow associated with changes in entropy was found to be nearly identical for both electrolyte blends, as would be expected since the electrode materials are nominally identical for machine-made pouch cells. Both cells show a large entropic heat flow beginning above 4.2 V. This can be understood with a simple lattice gas model^{57–60} of the cathode, where the configurational entropy decreases dramatically as small amounts of lithium are removed from the already highly delithiated cathode material (the rate of change of lithium content is negative, resulting in an endothermic heat flow).

Figure 5 also shows that below 4.2 V, cells containing 2% VC and PES211 have very similar parasitic heat flows that increase minimally as a function of potential. Between 4.2 V and 4.3 V, the heat flow due to parasitic reactions begins to increase dramatically for both electrolytes. As an order of magnitude reference point, a sustained parasitic heat flow of 100 $\mu\text{W}/\text{Wh}$ would consume all the electrolyte in these cells within one year.⁴⁸ Above 4.3 V, the parasitic heat flow continues to increase very rapidly, but the addition of the PES211 additive blend reduces the parasitic heat flow as compared to the cell containing 2% VC. The rapid increase in parasitic heat flow above 4.2 V suggests that the highly delithiated cathode surface becomes very reactive toward the electrolyte at high potentials. This is one reason why cells cycled above 4.2 V showed worse capacity retention than those cycled to lower upper cutoff potentials. It is not easy to explain why the cells with PES211 show worse capacity retention than those with 2% VC based on the microcalorimetry results alone, which predict the opposite. Detailed knowledge of the reaction products, in addition to the rate of parasitic heat generation is required.

In order to explore if there is any serious structural change of NMC811 during charge/discharge and whether this change has a significant impact on the cells for long term cycling at the rates tested, a series of in-situ and ex-situ experiments were performed.

Figure 6 shows the diffraction patterns from the in-situ XRD experiments with a sequential offset in intensity for clarity. The right

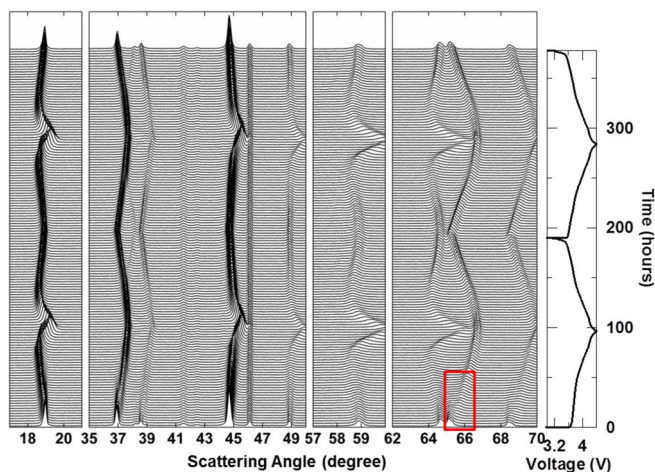


Figure 6. Diffraction patterns from in-situ XRD experiments, displayed with a sequential offset in intensity for clarity. The right panel shows the voltage curve of the cell as a function of time, which is aligned with the diffraction patterns. The cells were cycled between 3.0–4.4 V at a rate of C/100 for two cycles. Each XRD scan took about 2.5 h.

panel shows the voltage curve of the cell as a function of time, which is aligned with the diffraction patterns. The cells were charged and discharged between 3.0–4.4 V at a rate of C/100 for two cycles, while each XRD scan was about 2.5 h. The crystal structure of the material can be indexed in a R^3m space group. As the diameter of the active material coated on the beryllium window was smaller than the beam width at lower angles, the intensity of the detected (003) peak was much lower than expected. The (003) reflection at about 18.96° continually shifted to lower scattering angle during the first charge, however, it began to shift rapidly to higher scattering angle after the cell reached ~ 4.0 V. The scattering angle was $\sim 19.09^\circ$ when the cell eventually reached 4.4 V, indicating a significant decrease in the c-axis of the hexagonal structure between 4.0 V and 4.4 V. Moreover, the scattering angle decreased rapidly at the beginning of discharge to ~ 4.0 V and then gradually increased to $\sim 18.93^\circ$ when the cell was eventually discharged to 3.2 V. This process was mostly reversible during the second cycle. A similar trend was observed for the (104) peak at $\sim 44.5^\circ$, the (015) peak at $\sim 48.8^\circ$ and (108) reflection at $\sim 64.6^\circ$. The (110) peak at $\sim 65.12^\circ$, as highlighted in the red box, gradually disappeared at the beginning of the first charge, which cannot be observed in the same position after the cell was discharged to 3.2 V, nor in subsequent cycles. Meanwhile, a new peak at a higher angle (near 65.3°) appeared at the beginning of the first charge and a new (110) peak at $\sim 65.19^\circ$ was detected at the end of the first and second discharges. This indicates that there was a two hexagonal phase co-existence region at the beginning of the first charge. Figure S2 in the supporting information shows a two-phase Rietveld refinement during this coexistence region during the first charge. The structure changed in a different way at the beginning of the second charge where only single phase behavior was observed. This agrees well the electrochemical results of the half cells shown in Figure 1, where the voltage and dQ/dV curves were different for the first charge and second charge in the 3.0–3.9 V region.

Rietveld refinements were performed on the data assuming one/two hexagonal layered phases in the R^3m space group (α -NaFeO₂-type structure) to extract the lattice information. It was assumed that Li was on the 3a sites (lithium layer), transition metals were on the 3b sites (transition metal layer), and oxygen was on the 6c sites. The exchange of Ni and Li atoms between 3a and 3b sites was allowed with constraints such that the stoichiometry of the phase was fixed to the values assumed from the target composition. Preferred orientation parameters were fit in order to compensate for the low intensity of the (003) peak, which will not significantly impact the extraction of the peak position and lattice constant.

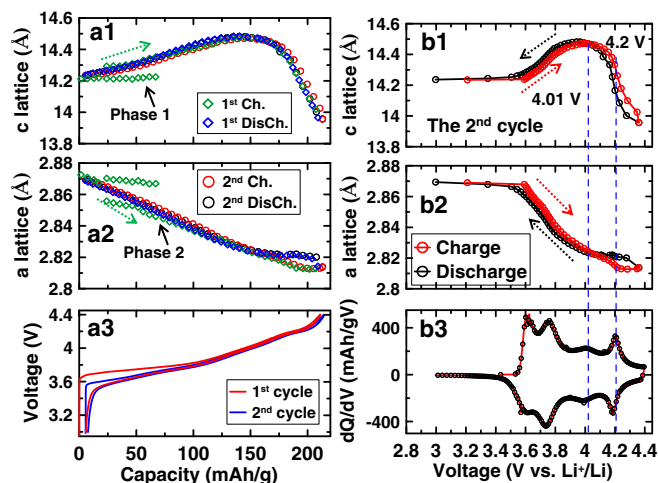


Figure 7. The c-axis (a1), a-axis (a2) and the potential of the in-situ cell (a3) as a function of specific capacity. The c-axis (b1) and a-axis (b2) as a function of cell potential during the second cycle, and dQ/dV of the second cycle as a function of cell potential (b3).

Figures 7a1 and 7a2 show the c-axis and a-axis lattice constants as a function of the specific capacity, respectively, while Figure 7a3 shows the voltage of the in-situ cell as a function of the specific capacity of the cell. The green diamonds show the first charge and the blue diamonds show the first discharge, while the red circles show the second charge and the black circles show the second discharge. The green dashed arrow indicates the direction of the change starting from the first charge. It shows that the initial c and a lattice constants were ~ 14.21 Å and 2.873 Å, respectively, which were slightly different than the lattice constants (14.20, 2.871) Å that were directly obtained from the powder samples due to the off-axis displacement of the in-situ electrode.

There was a two phase co-existence region at the beginning of the first charge, which has been discussed in the previous sections, where the two phases called phase 1 and phase 2 are identified with black arrows in Figures 7a1 and 7a2, respectively. At the beginning of charge, phase 1 showed a relatively larger a-axis lattice constant than that for phase 2.

With further charging of the cell, phase 1 disappeared while the c-axis of phase 2 kept increasing to ~ 14.49 Å when the capacity reached ~ 150 mAh/g. However, upon further charging of the cell, it began to dramatically decrease. The c-axis was ~ 13.96 Å at the end of the first charge when the capacity was ~ 210 mAh/g. The a-axis of phase 2 smoothly decreased during the whole charge process. The change of the lattice constants for phase 2 was reversible in the following cycles. The lattice constants of the active material at the end of the first discharge were about (2.870, 14.23) Å.

Figures 7b1 and 7b2 show the c and a axes as a function of cell potential for the second cycle, while Figure 7b3 shows dQ/dV of the second cycle as a function of cell potential. The red circles show the data for the second charge and the black circles show the data for the second discharge. The color-matched arrows indicate the direction of change for the charge and discharge processes. The c-axis continually increased from 14.23 Å to 14.47 Å until the cell potential reached 4.01 V (first vertical blue dashed line). It then started to smoothly decrease with further increase of cell potential. However, a rapid drop in the c-axis (13.96 Å at 4.4 V) was observed after the cell potential reached 4.2 V (second vertical blue dashed line). The a-axis gradually decreased with increasing potential throughout the charge process. This change in the lattice parameters with potential was mostly reversible, though a small hysteresis was detected between charge and discharge above 4.2 V. Figure S3 in the supporting information shows

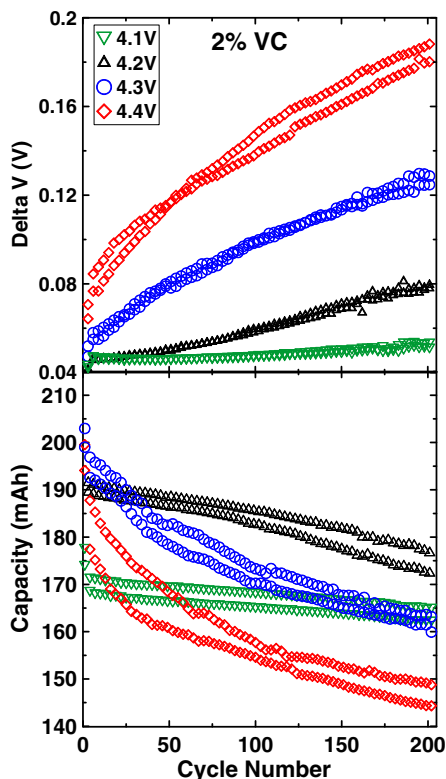


Figure 8. Capacity (a) and ΔV (b) of 2% VC cells as a function of cycle number for 200 cycles at a rate of C/5 in a temperature box at 30°C.

the percentage changes of the lattice constants as a function of voltage during the second cycle.

The dramatic change of the c-axis at higher potential could lead to the cracking of particles and poor connections between particles as well as macrostrains⁶¹ in the electrode after extensive cycling, which might be one of the reasons for the poor cycling performance of cells that cycled to a potential higher than 4.2 V. In order to confirm if this could be the case for the NMC811 cells, pouch cells with 2% VC were cycled for 200 cycles. The active materials were carefully recovered after discharging the cell to ~ 0 V for ex-situ experiments. This is very important as it is meaningless for comparison if the cells were at different states of charge.

Figure 8 shows (a) the capacity and (b) ΔV of the 2% VC pouch cells as a function of cycle number for 200 cycles at a rate of C/5 for tests at 30°C. Cells were cycled to varying upper cutoff potentials of 4.1 V, 4.2 V, 4.3 V, and 4.4 V, which are shown with green inverted triangles, black triangles, blue circles and red diamonds respectively. Figure 8a shows that the capacity for cells cycled to 4.1 V, 4.2 V, 4.3 V and 4.4 V after 200 cycles was 163 mAh, 175 mAh, 162 mAh, and 146 mAh corresponding to a capacity retention of 96%, 91%, 83% and 80%, respectively, comparing to the second discharge capacity at C/5. Figure 8b shows that ΔV for cells cycled to 4.1 V, 4.2 V, 4.3 V and 4.4 V after 200 cycles was ~ 0.052 V, 0.077 V, 0.126 V and 0.184 V respectively. A larger value and more rapid increase in ΔV were detected for the cells that cycled to a higher potential.

Figure 9 shows SEM images of the fresh electrode (a1, a2), and recovered electrodes that were cycled to upper cutoff potentials of 4.1 V (b1, b2), 4.2 V (c1, c2), 4.3 V (d1, d2) and 4.4 V (e1, e2) after 200 cycles at a rate of C/5. Images of the NMC811 cathode particles with lower magnification are shown on the left and images with higher magnification are shown on the right. The images of the electrodes cycled to 4.1 V, 4.2 V, 4.3 V and 4.4 V were very similar to those of the fresh electrodes. No significant damage to either electrode, such as particle cracking or disconnections between particles, was observed from these top-view SEM results

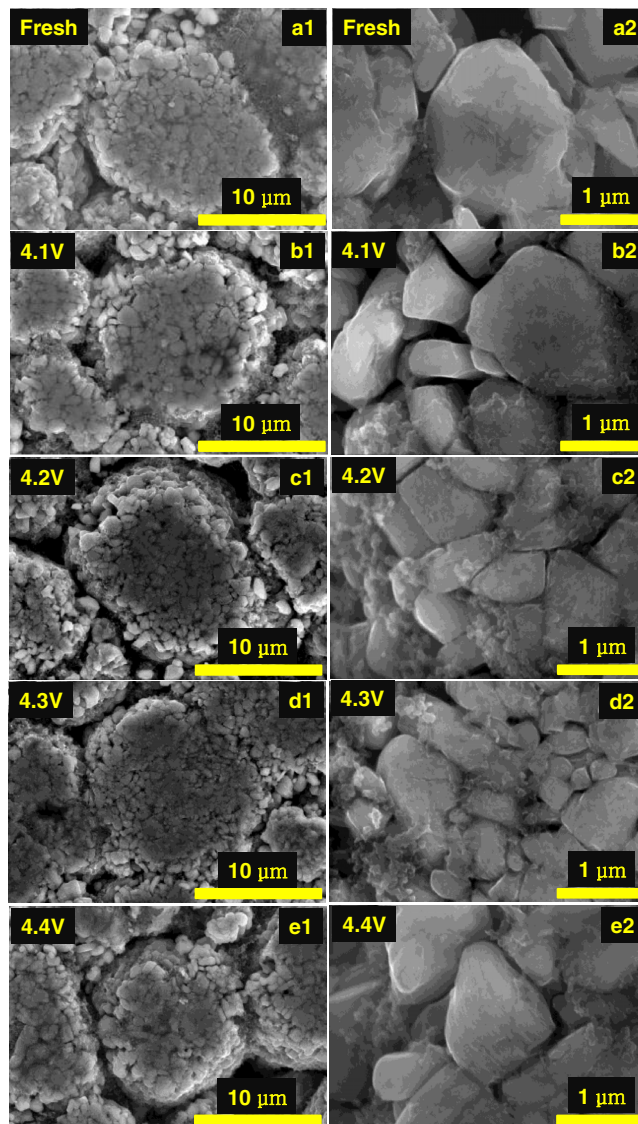


Figure 9. SEM images of the fresh NMC811 electrode (a1, a2), and recovered electrodes that were cycled to 4.1 V (b1, b2), 4.2 V (c1, c2), 4.3 V (d1, d2) and 4.4 V (e1, e2).

Figure 10 shows XRD patterns of the fresh electrode (A) and the recovered electrodes that were cycled to 4.1 V (B), 4.2 V (C), 4.3 V (D) and 4.4 V (E), respectively. The black symbols show the collected data and the red lines are the fits to the data for a $R\bar{3}m$ space group. The right panel shows an expanded view of the (104) reflections. There were no observable differences in either the peak shape or position between electrodes which were cycled to different upper cutoff potentials. The results of the refinements are presented in Table I. The fresh electrode had lattice constants of (2.8710, 14.204) Å, which were the same as those measured from the NMC811 powder within uncertainty. The recovered electrode that was cycled to 4.1 V (A) had lattice constants of (2.8711, 14.216) Å. There was slight increase in the c-axis compared to that of the fresh electrode due to the change that occurs after the first charge that was observed in the in-situ results. The c-axes of the recovered electrodes that were cycled to 4.2 V, 4.3 V and 4.4 V were 14.217 Å, 14.217 Å, and 14.221 Å, respectively, which are consistent with that of electrode A (4.1 V) within uncertainty (0.004 Å). The a-axes increased slightly for the recovered electrodes that were cycled to higher potentials (4.3 and 4.4 V). Additionally, there was no significant difference in the Ni

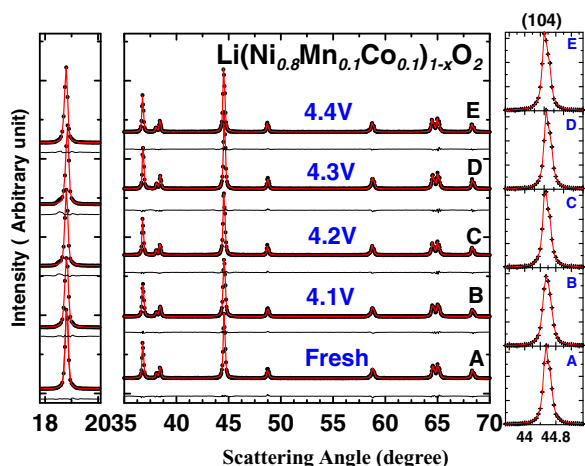


Figure 10. XRD patterns of the fresh NMC811 electrode (A) and the recovered electrodes that were cycled 200 times to 4.1 V (B), 4.2 V (C), 4.3 V (D) and 4.4 V (E), respectively. The right panel shows an expanded view of the (104) reflection.

content in the lithium layer. Electrode A (4.1 V) showed a slightly larger full width at half maximum (FWHM) at 44.5°, while it was very close for the other electrodes (C, D and E). The recovered electrodes that were cycled to higher potentials (4.3 and 4.4 V) did not show any significant structural differences compared to the recovered electrodes that were cycled to lower potentials (4.1 and 4.2 V).

Previous results showed that there was a large *c* axis contraction and expansion at high potentials during charge and discharge processes. However, the results presented in Figures 9, 10 and Table I show that this did not cause any significant morphological changes to the electrodes or the atomic structure of the recovered active material after extensive cycling at a rate of C/5 and temperature of 30.0°C. The structural changes in the active material during charge and discharge may not be the major contributor to the poor cycling performance of the cells cycled at high potentials. Instead, we suggest it is the onset of severe parasitic reactions between electrode material and electrolyte above 4.2 V (as shown by Figure 5) that is responsible for the poor capacity retention for cells cycled to 4.3 or 4.4 V.

Figure 11 shows the self-heating rate (SHR) versus temperature for charged NMC811 (4.2 V) and charged NMC111 (4.2 V) with control electrolyte tested between 70°C and 350°C, which are shown in blue and black lines respectively. The dashed lines show results from duplicate samples. An exothermic onset was detected at around 105°C for NMC811 samples, while it was not observed for NMC111 samples up to about 200°C. Additionally, the SHR for NMC811 samples increased rapidly after about 120°C, which was much higher than that for NMC111 at the same temperature. The SHR at 200°C was about 1°C/min for NMC811 whereas it was ~0.05°C/min for NMC111. The delithiated NMC811 samples showed severe reactivity with the control electrolyte at elevated temperature. This suggests that NMC811/graphite cells may be very difficult to design to pass

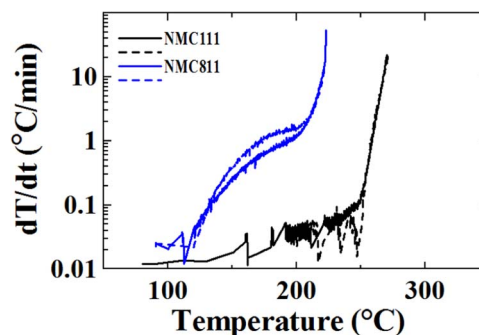


Figure 11. Self-heating rate (SHR) versus temperature for delithiated NMC811 (blue) and NMC111 (black) with control electrolyte tested between 70°C and 350°C.

mandatory Li-ion cell safety tests such as the oven exposure test, among others. It will probably be necessary to modify the cathode surface and/or identify and use electrolyte blends to dramatically improve the safety of NMC811 electrodes.

Conclusions

NMC811 can deliver a high capacity of ~200 mAh/g with an average discharge potential of ~3.9 V (vs. Li⁺/Li), which could be a promising cathode electrode material for high energy density lithium ion batteries. However, electrochemical tests from NMC811/Li coin cells and NMC811/graphite pouch cells showed poor cycling performance for cells that were cycled to potentials greater than 4.2 V. Pouch cells containing control electrolyte with 2% VC showed much better capacity retention and lower ΔV than cells with PES211 when cycled to the same upper cutoff potentials. However, severe impedance growth was observed for all the cells that cycled to above 4.2 V. Isothermal micro-calorimetry results showed that the parasitic heat flow increased as a function of potential, dramatically so above 4.2 V, for both 2% VC and PES211 cells. A significant *c*-axis contraction from ~14.47 Å to ~13.96 Å during charging between 4.0–4.4 V was measured using in-situ XRD. However, no significant changes of the morphology of the electrodes or the atomic structure of the recovered active materials after 200 cycles at a rate of C/5 were observed from the top-view ex-situ SEM, and ex-situ XRD results. The dramatic structural change of the active material during charge and discharge may not be the major contributor to the poor cycling performance of the cells that cycled to higher potentials. The parasitic reactions that arise from the interactions between the electrolytes and the highly reactive delithiated cathode surface at high potentials are suggested to be responsible for the failure of cells cycled to above 4.2 V. Charged NMC811 showed much stronger reactivity with electrolyte than NMC111 at elevated temperatures suggesting it may be difficult to prepare NMC811 Li-ion cells that can pass mandatory safety tests such as the oven exposure test. It is essential to improve the performance of NMC811 at high potentials by modifying the cathode surface and/or identifying and using electrolyte blends which reduce parasitic reactions and improve safety.

Table I. Rietveld refinement results of the recovered electrodes.

NMC811						
ID	Sample	a (Å) (± 0.0001)	c (Å) (± 0.004)	Ni _{Li} (%)	FWHM (44.5°)	Bragg R-factor
	Powder sample	2.8708	14.202	3.0	0.128	3.01
A	Fresh electrode	2.8710	14.204	1.1	0.139	2.14
B	4.1 V (200 cycles)	2.8711	14.216	0.76	0.188	3.15
C	4.2 V (200 cycles)	2.8717	14.217	1.26	0.128	2.46
D	4.3 V (200 cycles)	2.8722	14.217	0.94	0.122	3.34
E	4.4 V (200 cycles)	2.8721	14.221	1.26	0.125	1.79

References

- Z. Chen, Z. Lu, and J. R. Dahn, *J. Electrochem. Soc.*, **149**, A1604 (2002).
- A. J. Smith, J. C. Burns, S. Trussler, and J. R. Dahn, *J. Electrochem. Soc.*, **157**, A196 (2010).
- A. J. Smith, J. C. Burns, and J. R. Dahn, *Electrochem. Solid-State Lett.*, **13**, A177 (2010).
- A. J. Smith, J. C. Burns, X. Zhao, D. Xiong, and J. R. Dahn, *J. Electrochem. Soc.*, **158**, A447 (2011).
- A. J. Smith, J. C. Burns, D. Xiong, and J. R. Dahn, *J. Electrochem. Soc.*, **158**, A1136 (2011).
- A. W. Rowe, J. Camardese, E. McCalla, and J. R. Dahn, *J. Electrochem. Soc.*, **161**, A1189 (2014).
- D. Y. Wang et al., *J. Electrochem. Soc.*, **161**, A1818 (2014).

8. D. Y. Wang, N. N. Sinha, J. C. Burns, R. Petibon, and J. R. Dahn, *J. Power Sources*, **270**, 68 (2014).
9. D. Y. Wang, A. Xiao, L. Wells, and J. R. Dahn, *J. Electrochem. Soc.*, **162**, A169 (2014).
10. K. Xu, *Chem. Rev.*, **114**, 11503 (2014).
11. J. C. Burns et al., *J. Electrochem. Soc.*, **160**, A1451 (2013).
12. J. Camardese, J. Li, D. W. Abarbanel, T. B. a. Wright, and J. R. Dahn, *J. Electrochem. Soc.*, **162**, A269 (2014).
13. S.-T. Myung, H.-J. Noh, S.-J. Yoon, E.-J. Lee, and Y.-K. Sun, *J. Phys. Chem. Lett.*, **5**, 671 (2014).
14. J. Ju, E. Lee, C. S. Yoon, S. Myung, and Y. Sun, *J. Phys. Chem. C*, **118**, 175 (2013).
15. E. McCalla, A. W. Rowe, R. Shunmugasundaram, and J. R. Dahn, *Chem. Mater.*, **25**, 989 (2013).
16. E. McCalla, J. Li, A. W. Rowe, and J. R. Dahn, *J. Electrochem. Soc.*, **161**, A606 (2014).
17. C. R. Brown, E. McCalla, and J. R. Dahn, *Solid State Ionics*, **253**, 234 (2013).
18. C. Brown, *Master's thesis, Dalhousie Univ.* (2014).
19. X. Xiang, J. C. Knight, W. Li, and A. Manthiram, *J. Phys. Chem. C*, 21826 (2014).
20. J. Liu and A. Manthiram, *J. Mater. Chem.*, **20**, 3961 (2010).
21. K. A. Jarvis, Z. Deng, L. F. Allard, A. Manthiram, and P. J. Ferreira, *Chem. Mater.*, **23**, 3614 (2011).
22. C. R. Fell et al., *Chem. Mater.*, **25**, 1621 (2013).
23. C. R. Fell, M. Chi, Y. S. Meng, and J. L. Jones, *Solid State Ionics*, **207**, 44 (2012).
24. J. Li, J. Camardese, S. Glazier, and J. R. Dahn, *Chem. Mater.*, **26**, 7059 (2014).
25. J. Bréger et al., *J. Solid State Chem.*, **178**, 2575 (2005).
26. I. Hwang, C. W. Lee, J. C. Kim, and S. Yoon, *Mater. Res. Bull.*, **47**, 73 (2012).
27. Z. Lu, L. Y. Beaulieu, R. A. Donabarger, C. L. Thomas, and J. R. Dahn, *J. Electrochem. Soc.*, **149**, A778 (2002).
28. Z. Lu and J. R. Dahn, *J. Electrochem. Soc.*, **149**, A815 (2002).
29. Z. Lu and J. R. Dahn, *J. Electrochem. Soc.*, **148**, A237 (2001).
30. Z. Lu, D. D. MacNeil, and J. R. Dahn, *Electrochem. Solid-State Lett.*, **4**, A191 (2001).
31. D. Mohanty et al., *J. Power Sources*, **229**, 239 (2013).
32. A. W. Rowe and J. R. Dahn, *J. Electrochem. Soc.*, **161**, A308 (2013).
33. K. A. Jarvis, Z. Deng, L. F. Allard, A. Manthiram, and P. J. Ferreira, *J. Mater. Chem.*, **22**, 11550 (2012).
34. H. Koga et al., *J. Phys. Ch.*, **116**, 13497 (2012).
35. M. Gu et al., *ACS Nano*, **7**, 760 (2013).
36. M. O. Lai, L. Lu, Bohang Song, and Zongwen Liu, *Phys. Chem. Chem. Phys.*, **14**, 12875 (2012).
37. E.-S. Lee and A. Manthiram, *J. Mater. Chem. A*, **2**, 3932 (2014).
38. M. N. Ates et al., *J. Electrochem. Soc.*, **161**, A290 (2013).
39. H. Koga et al., *J. Power Sources*, **236**, 250 (2013).
40. A. Boulineau, L. Simonin, J.-F. Colin, C. Bourbon, and S. Patoux, *Nano Lett.*, **13**, 3857 (2013).
41. H.-J. Noh, S. Youn, C. S. Yoon, and Y.-K. Sun, *J. Power Sources*, **233**, 121 (2013).
42. R. J. Gummow, N. Sharma, R. Feng, G. Han, and Y. He, *J. Electrochem. Soc.*, **160**, A1856 (2013).
43. D.-H. Cho et al., *J. Electrochem. Soc.*, **161**, A920 (2014).
44. Y.-K. Sun, D.-J. Lee, Y. J. Lee, Z. Chen, and S.-T. Myung, *ACS Appl. Mater. Interfaces*, **5**, 11434 (2013).
45. J.-H. Shim et al., *Electrochim. Acta*, **138**, 15 (2014).
46. M.-H. Kim, H.-S. Shin, D. Shin, and Y.-K. Sun, *J. Power Sources*, **159**, 1328 (2006).
47. C.-H. Jo et al., *Nano Res.*, 1 (2014).
48. L. E. Downie and J. R. Dahn, *J. Electrochem. Soc.*, **161**, A1782 (2014).
49. L. Ma, J. Xia, X. Xia, and J. R. Dahn, *J. Electrochem. Soc.*, **161**, A1495 (2014).
50. H. Shi et al., *J. Alloys Compd.*, **587**, 710 (2014).
51. W. Li, J. N. Reimers, and J. R. Dahn, *Solid State Ionics*, **67**, 123 (1993).
52. J. Jiang, K. W. Eberman, L. J. Krause, and J. R. Dahn, *J. Electrochem. Soc.*, **152**, A1879 (2005).
53. L. Ma, J. Xia, X. Xia, and J. R. Dahn, *J. Electrochem. Soc.*, **161**, A1495 (2014).
54. L. Ma, J. Xia, and J. R. Dahn, *J. Electrochem. Soc.*, **161**, A2250 (2014).
55. L. M. J. R. D. and Jian Xia, *J. Power Sources* (2014).
56. L. E. Downie, S. R. Hyatt, A. T. B. Wright, and J. R. Dahn, *J. Phys. Chem. C*, **118**, 29533 (2014).
57. V. I. Kalikmanov and S. W. De Leeuw, **155**, 195 (2002).
58. V. I. Kalikmanov, M. V. Koudriachova, and S. W. De Leeuw, **137**, 1373 (2000).
59. W. R. McKinnon, *Solid State Commun.*, **40**, 343 (1981).
60. W. R. McKinnon, *thesis, Univ. Brit. Col.* (1980).
61. K. Amine and Y. Sun, *Nano Lett.*, **14**, 4873 (2014).